Multifunctional organic-inorganic hybrid films deposited by the Langmuir-Blodgett technique

Akhtar, Naureen

Chapter 5

Design of Molecule-Based Magnetic Conductors[#]

Molecule-based conducting magnets where the conduction electrons originate from an organic component and magnetism from an inorganic building block have been an area of great interest in the view of unconventional coexistent multifunctional properties. For the creation of such molecular systems, organic donor tetrathiafulvalene derivatives are promising building blocks that can combine with variety of magnetic ions leading to π electron-d/f spin interaction systems. In this chapter we report on the deposition of thin hybrid films comprising arachidic acid and donor bis(ethylenedioxy)tetrathiafulvalene (BEDO-TTF) as organic component and Cu/Gd complexes as inorganic component by the Langmuir-Blodgett technique. From X-ray diffraction and transmission electron microscopy, we found that these films are crystalline with distinct organic and inorganic sublattices, where the BEDO-TTF molecular layer is interfaced with the inorganic layer. Due to the flexibility of the Langmuir Blodgett deposition technique, this result indicates the way for preparing films with various functionalities, determined by the choice of the inorganic compound that is combined with the π-unit of BEDO-TFF.

[#] This chapter is based on Naureen Akhtar, Graeme Blake, Roberto Felici, Heinz Amenitsch, Xiaoxing Ke, Gustaaf Van Tendeloo, Thomas T.M. Palstra and Petra Rudolf, "*Design of Molecule-Based Magnetic Conductors*" ready for submission.

5.1. Introduction

The design of the novel materials that combine two or more useful physical properties in one crystal or film is a focus of current research in materials science[1-3]. In layered structures each layer contributes its own physical properties but often new properties arise at the interface between layers; this allows for a design flexibility which is difficult or impossible to achieve in a continuous lattice[4]. In molecular materials a key issue is that local properties and cooperative phenomena depend on the arrangement of the molecules in the condensed phase[5]. In other words, the same molecules can exhibit significantly diverse physical properties in different packing arrangements because the intermolecular interactions are not the same. One such example is the organic donor bis(ethylenedithio)tetrathiafulvalene (BEDT-TTF) that in cation radical salts with the same counter ion presents electronic properties ranging from insulator to semiconductor to metal to superconductor[6-7].

Tetrathiafulvalene (TTF) and its derivatives have been extensively used to synthesize charge-transfer salts, giving rise to molecular conductors and superconductors[8-10]. These are the two-dimensional hybrid systems with a crystal structure where conducting radical cation layers alternate with inorganic anion ones. The π-π stacking of the adjacent molecules gives rise to intermolecular electronic transfer responsible for the transport properties. Organic-inorganic hybrids form a fascinating class of materials as they provide the opportunity of coexisting distinct properties originating from each constituent[11-13]. Moreover, the interaction between the sub-systems can lead to improved or exotic properties with respect to the individual constituents. For instance, the π-d interaction between the conducting and magnetic sub-systems leads to external field-induced superconductivity in λ-$(BETS)_2FeCl_4$ crystals[5].

Molecule-based hybrid materials are promising candidates for applications in molecular electronics[14-15]. However most of the hybrid materials studied so far have been prepared as crystals. Although these materials are very interesting model systems to tune the physical properties, processing techniques have to be developed to utilize them in devices. This involves the fabrication of these materials as thin films or nanoparticles. An old but elegant approach to arrange the molecules into organized assemblies with the possibility of built in architectural control at the monolayer level is the Langmuir Blodgett (LB) technique[16]. This layer-by-layer deposition method has been extensively used to fabricate supramolecular architectures on surfaces[17]. It permits to deposit not only regular organic amphiphiles but also to create useful complex structures wherein layers with controlled thickness[18-19] are

stacked in a desired sequence. However, the structure of such a complicated molecular system can be different from the expected one and needs to be carefully studied. In this chapter, we present a simple synthetic strategy for the preparation of novel organic-inorganic hybrid LB films where organic donor BEDO-TTF molecular layers with delocalized electrons are combined with sheets of magnetic ions (Gd/Cu) having localized spins. A series of analysis techniques were employed to investigate the structural properties of these films and thereby to demonstrate that this synthetic strategy is capable of precise control of the resulting material.

5.2. LB film deposition

BEDO-TTF was purchased from SYNCHEM. Arachidic acid (C_{20}), gadolinium acetate, copper chloride, and other chemical reagents of analytical grade were purchased from Aldrich and used as received. The subphase employed in the experiments was an aqueous solution of Gd/Cu ions, obtained by dissolving their corresponding precursors into water (20 mg/L). Ultra-pure ion free water with a resistivity of greater than 18 MΩcm was used for the preparation of subphase. Surface pressure-molecular area (∏-a) isotherm measurements and deposition experiments were performed using a NIMA Technology thermostated LB trough. The temperature was kept at 21 ^{o}C (25 ^{o}C) for the experiments with Gd (Cu) ions. Separate solutions of arachidic acid (8.22×10^{-4} mol/L) and BEDO-TTF (7.4×10^{-4} mol/L) in chloroform were mixed with a 1 : 2 molar ratio prior to being spread onto the subphase. After evaporation of the solvent, the molecules were compressed at a rate of 30 cm^2min^{-1} by a movable barrier until a desired surface pressure was reached and this pressure was kept constant during the whole deposition process. LB films were deposited by vertical dipping of hydrophobic substrates into the subphase at a dipping speed of 5 mm/min. A Langmuir film was deposited each time the substrate moved across the air-water interface. Hence, one dipping cycle (dipping down and lifting up the substrate from the subphase) gives two hybrid layers.

5.3. Results and discussion

5.3.1. ∏-a isotherm study of the Langmuir films

When a mixture of arachidic acid and BEDO-TTF is spread onto the subphase, BEDO-TTF molecules self-assemble into a layer just below the arachidic acid (C_{20}) molecular layer at the air-water interface through hydrogen bonding[20]. The formation of the hybrid Langmuir film was studied by recording ∏-a isotherms and by Brewster angle microscopy under

continuous compression. To better understand this multicomponent film, the Langmuir films of pure C_{20} and of a C_{20} + BEDO-TTF (1:2 molar ratio) mixture on a subphase of pure water were also studied[20].

Figure 5.1 shows the ∏-a isotherms of C_{20} on pure water, of C_{20} + BEDO-TTF on pure water, and of a C_{20} + BEDO-TTF mixture on a subphase containing metal ions. The lift-off area was calculated for each isotherm by extrapolating the linear section of the isotherm as shown in the inset of figure 5.1. As previously explained in Chapter 4, the isotherm of C_{20} showed a clear transition from the liquid to the solid phase around 25 mN/m, while for the C_{20} + BEDO-TTF Langmuir film, the occupied area per molecule is also determined by the lateral packing of the C_{20} molecules, although the shape of the isotherm is altered by the presence of BEDO-TTF molecules[20]. The transition from the liquid to the solid phase was no longer clearly distinguishable for the C_{20} + BEDO-TTF + Gd and C_{20} + BEDO-TTF + Cu Langmuir films. The isotherm of the C_{20} + BEDO-TTF+ Cu film revealed that it is highly compressible with a lift-off area of 26±1 $Å^2$. The higher lift-off area and the compressible character might be due to the penetration of Cu ions into the organic layer(s). The isotherm of the C_{20} + BEDO-TTF + Gd Langmuir film showed the steepest slope and the smallest lift-off area, indicating that a stable and well-packed film is formed at the air/water interface. The Gd ion is less likely to penetrate into the organic part of the film due to its large size.

The Brewster angle microscopy (BAM) images for all the four Langmuir films at various surface pressures are presented in figure 5.2. C_{20} and C_{20} + BEDO-TTF films on pure water showed the spontaneous creation of small islands right after solvent evaporation as evident from the brighter areas in figure 5.2 (a) and 5.2 (e), respectively. The C_{20} Langmuir film organized in small condensed islands with a domain structure typical of differently tilted orientations, as shown by the contrast in reflected intensity within the islands[21-22].

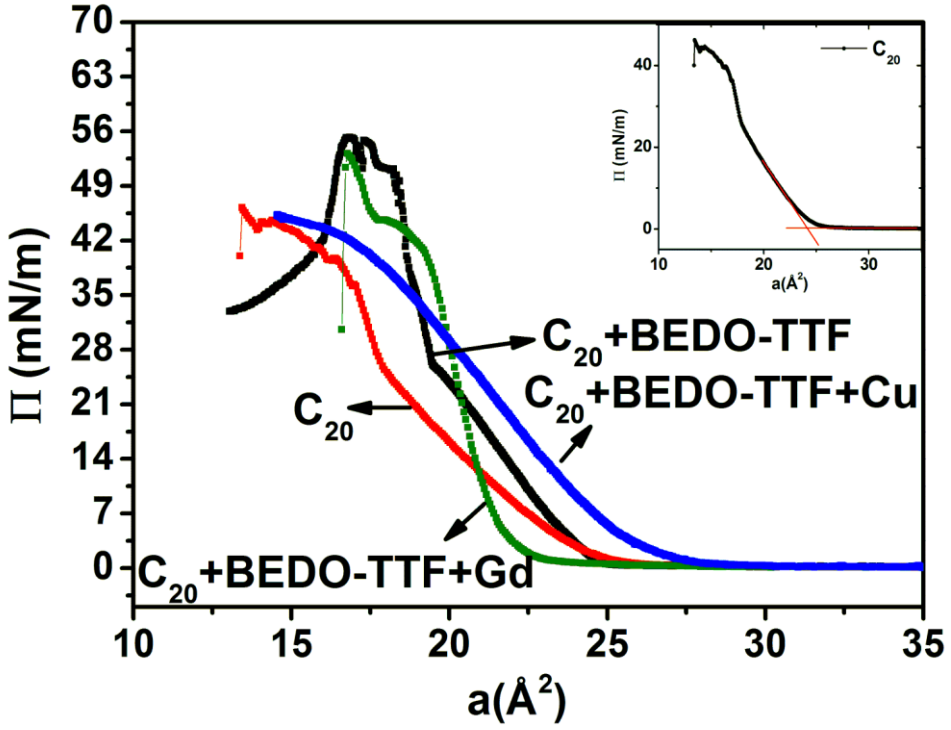

Figure 5.1. ∏-a isotherms of Langmuir films of pure C_{20}, C_{20}+BEDO-TTF, C_{20}+BEDO-TTF+Gd/Cu system. Inset: Illustration of determination of the lift-off area from the ∏-a isotherm of a pure C_{20} Langmuir film.

The domain size increased upon compression of the film and at the lift-off area most of the surface was covered with compact islands, as apparent in figure 5.2 (b). Compressing even further, the islands merge into bigger ones and the contrast of the domains within the islands gradually decreases[21]. This contrast of the domains was not detectable in the C_{20} + BEDO-TTF film, where the orientation of the C_{20} molecules is constrained by the presence of BEDO-TTF molecules. Such a 'knit-like' organization was also observed for the C_{18} + BEDO-TTF Langmuir films by H.Ohnuki *et al.*[23] Figure 5.2 (f) shows that this structure collapsed just above the lift-off area and upon further compression (∏ > 1 mN/m) a new structure appeared with a compact and homogeneous morphology (5.2 (g)). As shown in figure 5.2 (h), continuous and homogenous film was observed around 20 mN/m.

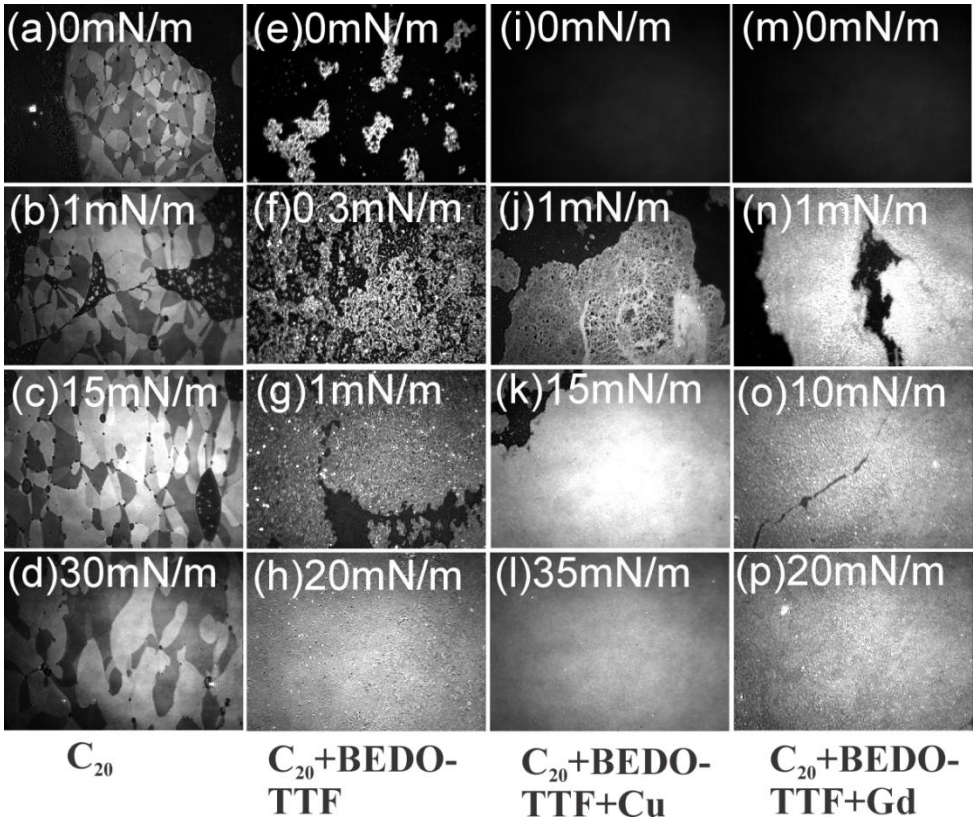

Figure 5.2. Brewster angle micrographs of Langmuir films of C_{20} on pure water (a-d), C_{20}+BEDO-TFF on pure water (e-h), C_{20}+BEDO-TTF on a subphase containing Cu/Gd (i-l/m-p) ions, taken at various surface pressures during continuous compression. Field of view is 720×400 μm^2.

For the C_{20} + BEDO-TTF + Cu and C_{20} + BEDO-TTF + Gd Langmuir films the first islands appeared around the lift-off area, as shown in the figure 5.2 (j) and 5.2 (n), respectively. The C_{20} + BEDO-TTF + Cu Langmuir film first exhibited a network of porous islands; compression eliminated the pores and when the surface pressure reached 15 mN/m the film structure had become compact and relatively homogenous, as apparent in figure 5.2 (k). This observation is in good agreement with the isotherm behaviour discussed above. Further compression caused the small islands to merge into bigger ones and a continuous film with uniform reflectivity formed at $\prod$ = 35mN/m, as evident in figure 5.2 (l). The C_{20} + BEDO-TTF + Gd Langmuir film showed highly compact small islands at the lift-off area

(figure 5.2 (n)); the size and number of these islands increased upon compression but their morphology remained same, as shown in figure 5.2 (o-p). This behaviour is reflected in the steep slope of the isotherm. The film could not be compressed beyond a molecular area of 20 $Å^2$ and collapsed around surface pressure of 36 mN/m.

5.3.2. X-ray photoelectron spectroscopy analysis of the multilayer LB films

X-ray photoelectron spectroscopy (XPS) was carried out on a 22-layer-thick hybrid LB film (built up in 11 dipping cycles) in order to identify the film composition and bonding of the constituent elements within the film structure. A survey spectrum of the hybrid LB films, presented in figure 5.3 (a), showed the photoemission lines of all the expected elements (C, O, S, Gd/Cu) which confirmed the presence of C_{20}, BEDO-TTF and the metal ions.

A detailed scan of Cu 2p and Gd 4d core level regions is displayed in figure 5.3 (b) and (c) respectively. Fitting of the Cu $2p_{3/2}$ line resulted in two components at binding energies of 934.8 eV and 936.2 eV, along with a broad shoulder appearing at ~8 eV higher binding energy than the main peak (figure 5.3 (b)). This broad feature is typical of Cu^{2+} giving rise to multiplet states[24]. The low binding energy component is assigned to Cu bonded to a hydroxyl group. The other component at higher binding energy is due to Cu bonded to the sulfur of the BEDO-TTF[25].

Photoemission from the Gd 4d shell leads to a $4d^9$ configuration. The onset of the main peak in Gd 4d spectrum appears at ~144 eV, indicating that the Gd ion is in the +3 oxidation state[26-27]. The second most intense peak is observed at ~7 eV above the onset of the main 4d envelope and due to multiplet states arising from the $4d^9$-$4f^7$ interaction. The coupling of the 4d core hole with the half-filled f shell leads to the main terms ^9D and ^7D and is as strong as the 4d spin orbit coupling[28]. The position of the most intense ^7D peak (~151 eV) is consistent with the literature values[29].

The XPS measurements were also performed on the organic LB film composed of C_{20} and BEDO-TTF alone. A detailed comparative study of the hybrid LB films with the organic LB film can give useful information on the film structure in terms of bonding of the metal ions. The spectra of the C 1s core level region for the three LB films is shown in figure 5.4 and revealed four components: aliphatic carbon at a binding energy of 285.2 eV and carboxylic carbon at 289.2 eV are contributed by the arachidic acid[30] while the other two components at 285.9 eV and 286.8 eV, are due to BEDO-TTF.

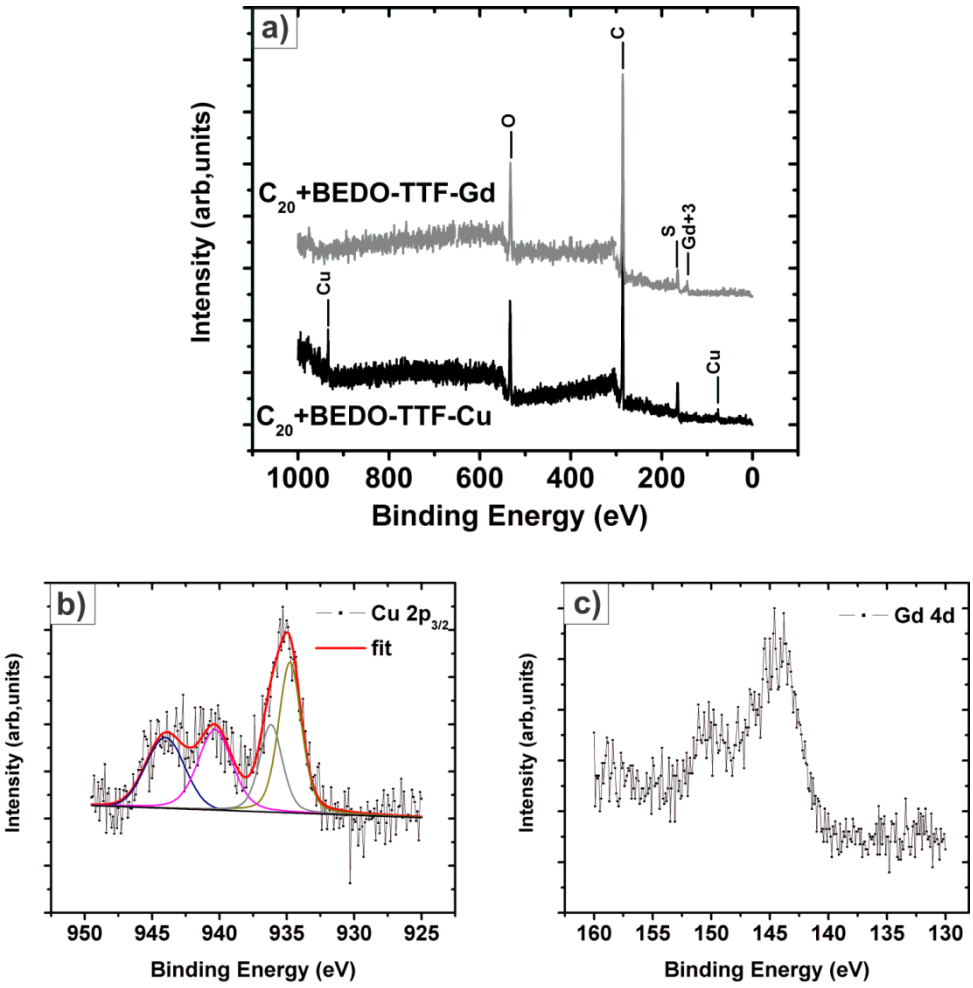

Figure 5.3. (a) X-ray photoemission survey spectra of 22-layer thick hybrid LB films. (b) X-ray photoemission spectra of the Cu $2p_{3/2}$ core level region of a C_{20} + BEDO-TTF + Cu LB film and (c) Gd 4d core level region of a C_{20} + BEDO-TTF + Gd LB film. The corresponding peak fitting results are also plotted.

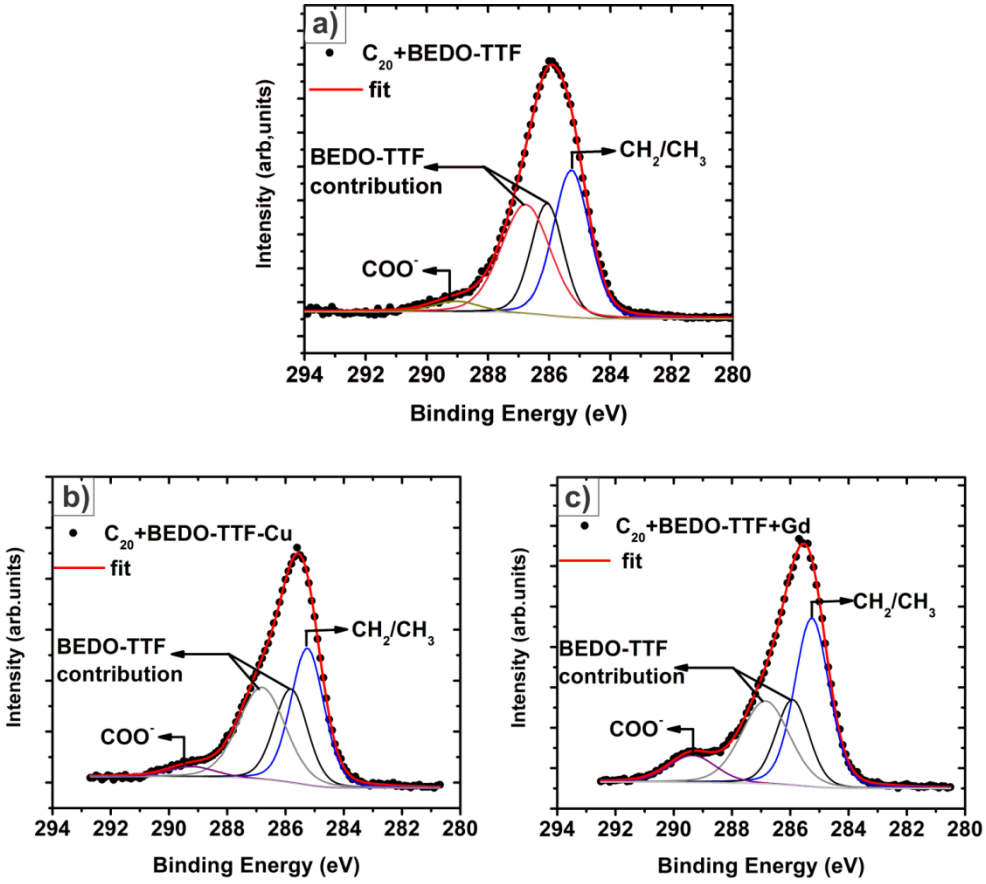

Figure 5.4. X-ray photoemission spectra of the C 1s core level region of 22-layer thick LB films prepared from C_{20}+BEDO-TTF (a), C_{20}+BEDO-TTF+Cu (b) and C_{20}+BEDO-TTF+Gd (c); the corresponding peak fitting results are also plotted.

The relative intensity of all the C 1s components of the C_{20} + BEDO-TTF + Cu LB film remained nearly same as for the C_{20} + BEDO-TTF film. However, as shown in figure 5.4 (c), in the spectrum of the C_{20} + BEDO-TTF + Gd LB film the intensity of the 289.2 eV component is higher, pointing to an increase in carboxylic carbon. This observation indicates the incorporation of the acetate from the subphase into the film.

The photoemission spectra of the oxygen 1s core level region for the hybrid LB films are shown in figure 5.5 together with that of the C_{20} + BEDO-TTF LB film; both contain three contributions: two come from the arachidic acid molecule, namely HO-C at a binding energy of 533.0 eV and O=C at 532.0 eV, and one from the BEDO-TTF ring oxygen at

534.0 eV. However, the deconvolution of the O 1s peak of the hybrid LB films revealed the presence of an additional component at lower binding energy.

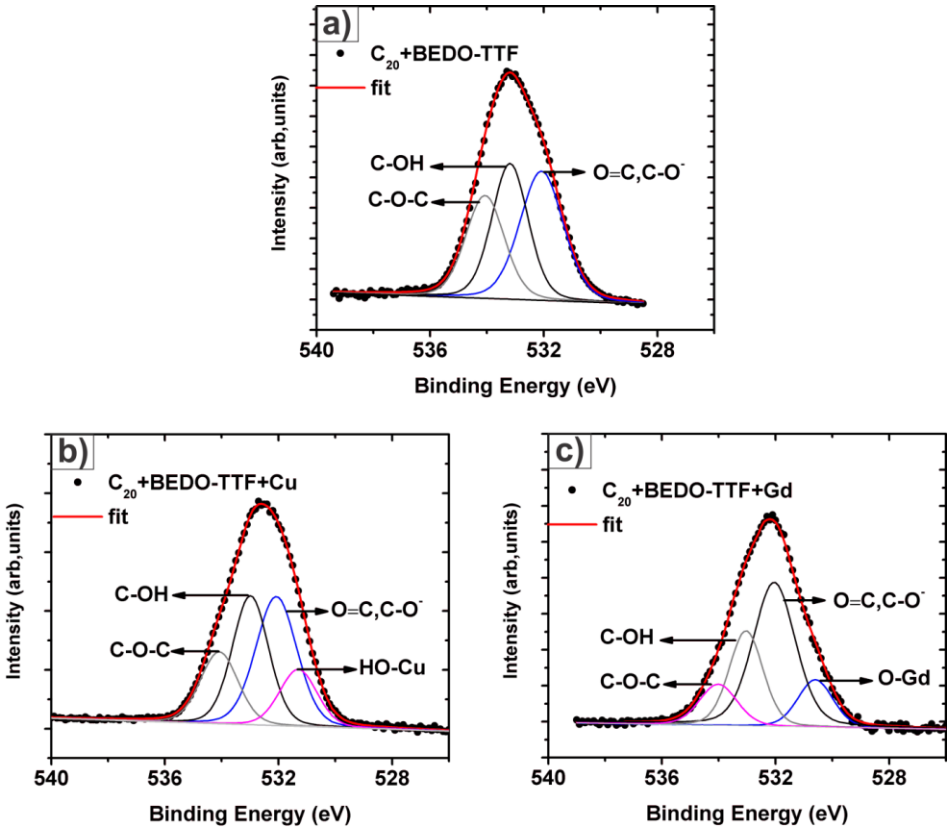

Figure 5.5. X-ray photoemission spectra of the O 1s core level region of 22-layer thick LB films prepared from C_{20}+BEDO-TTF (a), C_{20}+BEDO-TTF+Cu (b) and C_{20}+BEDO-TTF+Gd (c); the corresponding peak fitting results are also plotted.

For the C_{20} + BEDO-TTF + Cu film, this component appeared at 531.3 eV (figure 5.5 (b)) and is attributed to Cu bonded with hydroxyl species[25], while in the C_{20} + BEDO-TTF + Gd film an additional component appears at 530.6 eV, a binding energy which identifies it as due to Gd-O[31] (figure 5.5 (c)). Moreover, the relative intensity of the component at 532.0 eV increased with respect to the purely organic films, pointing to more C=O moieties in the C_{20}-BEDO-TTF-Gd film as already observed in the C 1s spectrum; this strengthens the hypothesis that Gd^{3+} is present in the film in the form of gadolinium acetate.

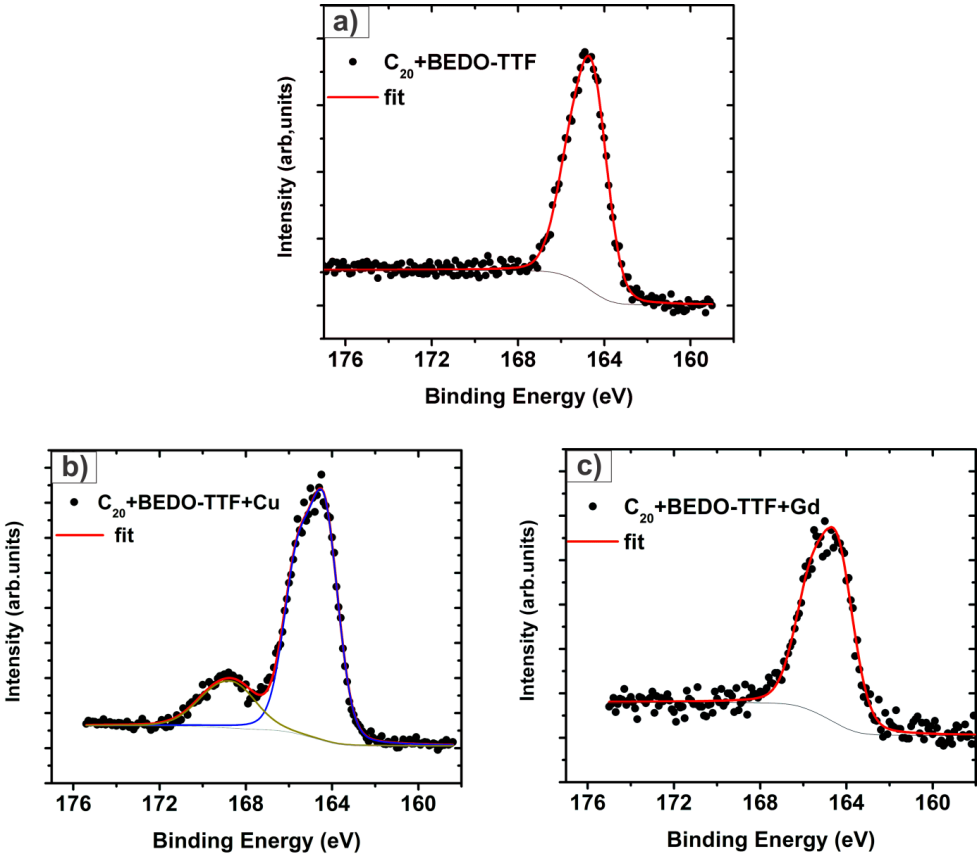

Figure 5.6. X-ray photoemission spectra of the S 2p core level region of 22-layer thick LB films prepared from C_{20}+BEDO-TTF (a), C_{20}+BEDO-TTF+Cu (b) and C_{20}+BEDO-TTF+Gd (c); the corresponding peak fitting results are also plotted.

Figure 5.6 shows the S 2p spectra for the hybrid LB films together with that of the C_{20} + BEDO-TTF LB film. The S 2p spectrum for the organic film was fitted with single doublet peaked at a binding of 164.7 eV which corresponds to the S-C bonds[32]. The spectrum of the C_{20} + BEDO-TTF + Gd LB film also showed the single component peaked at the same binding energy, while that of the C_{20} + BEDO-TTF + Cu LB film revealed an additional component at higher binding energy (168.8 eV). This component is due to Cu bonded to sulfur[33], a bond already identified in the discussion of the Cu 2p line.

5.3.3. Fourier transform IR spectroscopy

Fourier transform infrared spectra in the frequency range 700-4000 cm^{-1} were collected in reflectance mode on hybrid LB films to get further information on the tilting of organic molecules in the layer and on the partial charge transfer of the BEDO-TTF molecule. Figure 5.7 shows the spectra of six-layer LB films of C_{20} + BEDO-TTF (prepared from a mixture with 1:2 molar ratio), C_{20} + BEDO-TTF + Cu and C_{20} + BEDO-TTF + Gd. The most remarkable feature in the IR spectra of C_{20} + BEDO-TTF and C_{20} + BEDO-TTF + Cu LB films is the lower intensity of the symmetric (ν_s) and antisymmetric (ν_a) stretching modes of CH_2 as compared to that of C_{20} + BEDO-TTF + Gd film. Since these LB films were assembled on a gold substrate (see Chapter 2 for experimental details), the surface dipole selection rule applies and this intensity decrease indicates that the fatty acid molecules are standing up straight with respect to the film surface in the former.

All films showed a series of vibrational bands between 800 and 1200 cm^{-1}, mostly due to the vibrations including C-O bonds and characteristic of the mixed valence of BEDO-TTF molecules[34]. These vibrational features are very sensitive to the average charge on the donor molecule and shift towards lower frequency when the average charge on the donor increases[34]. The counter-anion in the C_{20} + BEDO-TTF films is the COO^- moiety of the fatty acid[23].

To estimate average charge on the BEDO-TTF molecule in our LB films, the values of the observed frequency shifts were compared to values recorded for different BEDO-TTF based salts where the degree of average charge transfer on the donor molecule ranges from +0.33 to +0.5[34]. In this way the average charge on BEDO-TTF was estimated as +0.4 e^- (+0.33 e^-) in C_{20} + BEDO-TTF and C_{20} + BEDO-TTF + Cu (C_{20} + BEDO-TTF + Gd) LB films. From this we conclude that in the C_{20} + BEDO-TTF and the C_{20} + BEDO-TTF + Cu LB films the molecular packing in the bilayer formed by C_{20} and BEDO-TTF is very similar resulting in a comparable average charge on the BEDO-TTF molecule.

In case of C_{20} + BEDO-TTF + Gd LB film the tilting of the arachidic acid leads to a smaller degree of charge transfer. In fact, a different orientation of C_{20} with respect to BEDO-TTF may alter the intermolecular separation within BEDO-TTF sheet and/or the distance between the C_{20} and the BEDO-TTF molecular layer; which of the two is responsible for the difference in charge transfer becomes evident from the X-ray diffraction data discussed below.

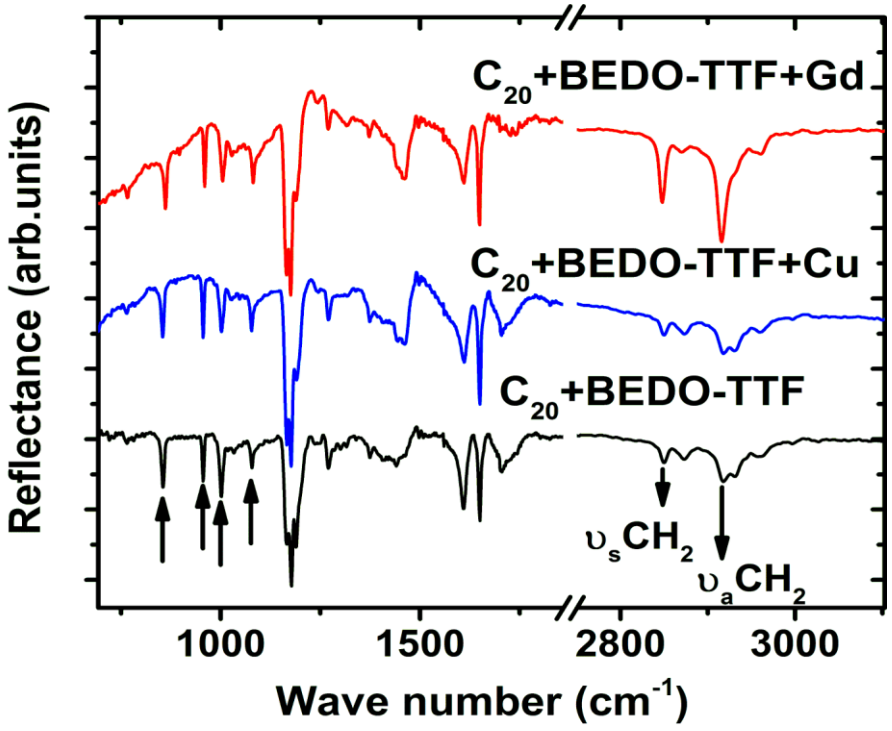

Figure 5.7. Infrared spectra of 6-layer thick C_{20} + BEDO-TTF, C_{20} + BEDO-TTF + Cu and C_{20} + BEDO-TTF + Gd LB films. See the text for the discussion of the vibrational bands indicated by arrows.

5.3.4. Structural analysis by X-ray diffraction

As already mentioned above, one layer consisting of C_{20}+BEDO-TTF + metal complex is deposited when a hydrophobic substrate is dipped into the subphase during the downward stroke and a second identical layer is transferred when lifting the substrate up again from the subphase in the upward stroke; this results in a Y-type deposition[16] as explained in Chapter 2. One dipping cycle (downstroke plus upstroke) is therefore expected to result in metal complexes sandwiched between the two C_{20} + BEDO-TTF bilayers as shown schematically in figure 5.8. A multilayer structure is obtained by repeating the dipping cycles. To verify whether the crystal structure of the hybrid LB films follows this scheme, X-ray diffraction experiments were performed on 22-layer thick films.

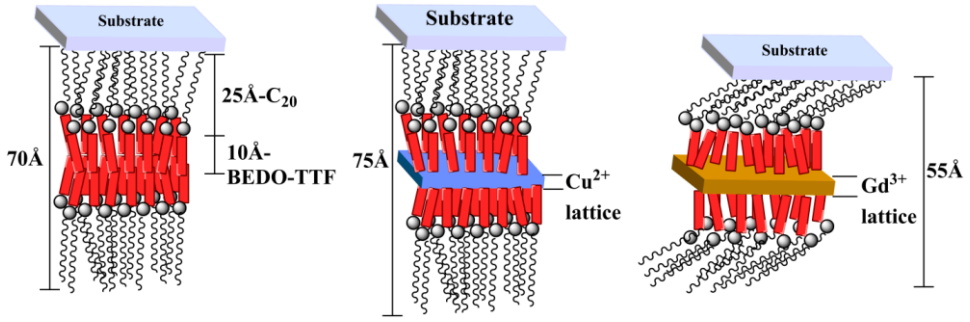

Figure 5.8. Schematic view of one repeat unit (one dip cycle) of the C_{20} + BEDO-TTF (left) C_{20} + BEDO-TTF + Cu (middle) and C_{20} + BEDO-TTF + Gd (right) LB films.

The out-of-plane X-ray reflectivity for 22-layer thick C_{20} + BEDO-TTF + Cu LB films deposited at various surface pressures is shown in figure 5.9. The Cu films were crystalline only when deposited at $\prod \geq 15$mN/m. The emergence of crystalline order at surface pressure of $\prod = 15$ mN/m is in good correspondence with the observation of compact film in BAM evident in figure 5.2 (k). The crystallinity improved with increasing surface pressure, implying better packing of the molecules with increasing pressure. Four diffraction peaks were observed for film deposited at $\prod = 35$ mN/m and indexed as 001, 002, 003, and 004. Using the diffraction condition $n\lambda = 2d \sin\theta$ for different orders n, the dimension of the periodic unit in the growth direction was found to be $d = 75\pm1$ Å. When a film was prepared without copper ions, $d = 70\pm1$ Å was found[20]. Clearly the copper ions are incorporated in the films; moreover, a spacing of this magnitude is consistent with a head-to-head, tail-to-tail configuration of the molecules in the films (Y-type deposition).

Figure 5.10 compares the out-of-plane X-ray reflectivity data for a C_{20} + BEDO-TTF + Cu LB film deposited at $\prod = 35$ mN/m with those of a C_{20} + BEDO-TTF + Gd LB film deposited at $\prod = 15$ mN/m. Diffraction studies on C_{20} + BEDO-TTF + Gd LB films deposited at different surface pressures (not shown here) revealed that these films were highly crystalline when deposited at $\prod = 15$ mN/m and the structural properties were the same for films deposited at higher $\prod$. The appearance of Kiessig fringes along with diffraction peaks in figure 5.10 indicate that the C_{20}+BEDO-TTF+Gd LB film remains relatively smooth during multilayer buildup[35]. However, the dimension of its periodic unit in the growth direction was found to be $d = 55\pm1$ Å, *i.e.* smaller than for the C_{20}+BEDO-TTF+Cu LB film. This indicates that the organic molecules are tilted away from the direction normal to the film plane in the former, in agreement with the infrared spectra discussed above.

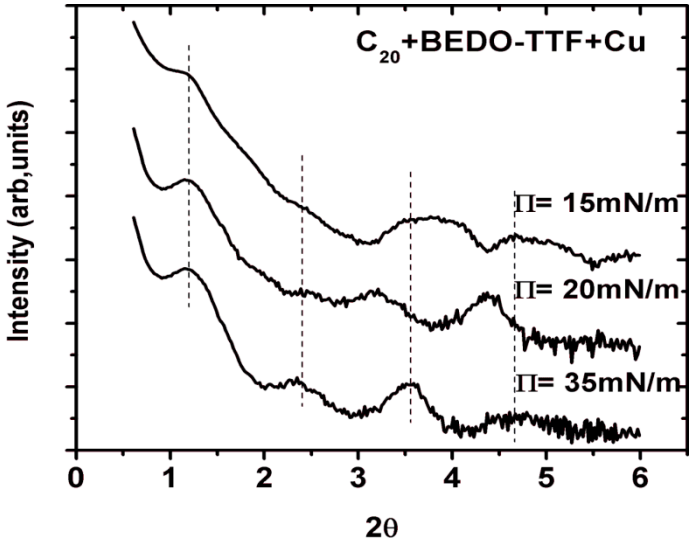

Figure 5.9. XRD patterns of 22-layer thick C_{20} + BEDO-TTF + Cu LB films deposited at various surface pressures as indicated.

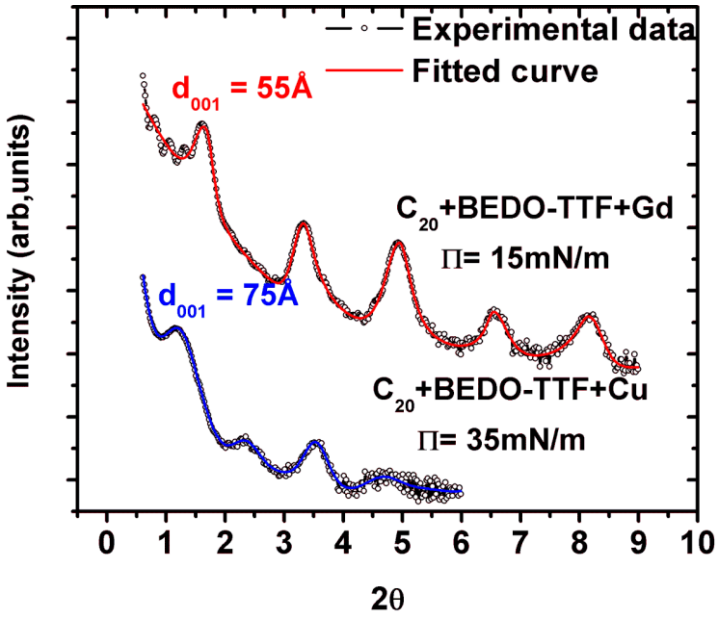

Figure 5.10. XRD patterns from 22-layer thick C_{20}+BEDO-TTF+Cu (bottom) and C_{20}+BEDO-TTF+Gd (top) LB films deposited at the indicated surface pressures.

Further information on the stacking of individual layers in these multilayer hybrid LB films was obtained from rocking curves (θ-scans) measured at the 001 peak position in the out-of-plane direction. The appearance of a single peak demonstrated that the individual layers are tidily stacked in both these hybrid films. The average tilt angle between the layers, as calculated from the FWHM of the rocking curves in figure 5.11, was 0.094±0.001° for the C_{20} + BEDO-TTF + Cu LB film and 0.038±0.0008° for the C_{20} + BEDO-TTF + Gd LB film. The smaller value for the Gd containing film indicates even better packing of the individual layers compared to the film with Cu complexes.

The in-plane diffraction patterns of the C_{20} + BEDO-TTF + Cu and C_{20} + BEDO-TTF + Gd LB films are shown in figure 5.12. In each case five peaks could be indexed, giving two-dimensional unit cells of a = 7.00±0.01 Å, b = 5.20±0.01 Å and γ = 87.1±0.1° for the C_{20} + BEDO-TTF + Cu LB film, and a = 7.00±0.01 Å, b = 5.25±0.01 Å and γ = 88.0±0.1° for C_{20} + BEDO-TTF + Gd LB film. For the Gd film there are two un-indexed peaks at 2θ = 6.50° and 10.80°. However, these are both much narrower than the indexed peaks and likely to originate from a different phase that we cannot identify from the current data. Similarly, un-indexed peaks appear in the XRD pattern of the Cu containing film at 2θ = 10.40° and 13.50°.

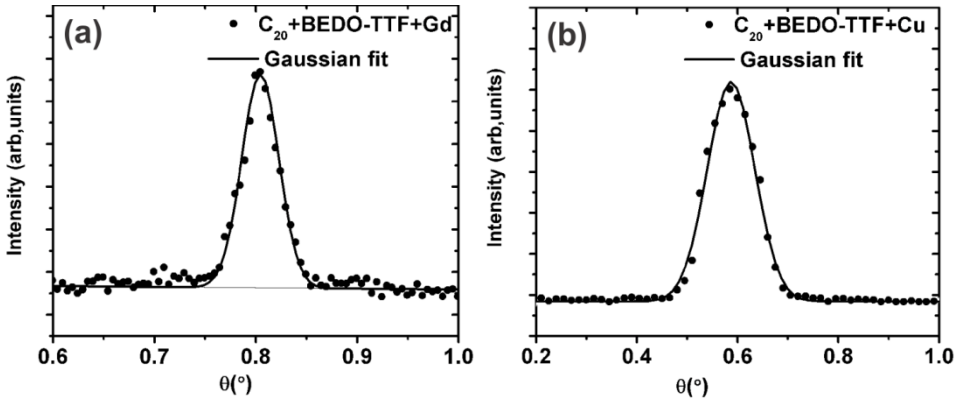

Figure 5.11. Rocking curves at the (001) peak position from 22-layer thick LB films of C_{20} + BEDO-TTF + Gd deposited at ∏ = 15 mN/m (a) and C_{20} + BEDO-TTF + Cu deposited at ∏ = 35 mN/m (b).

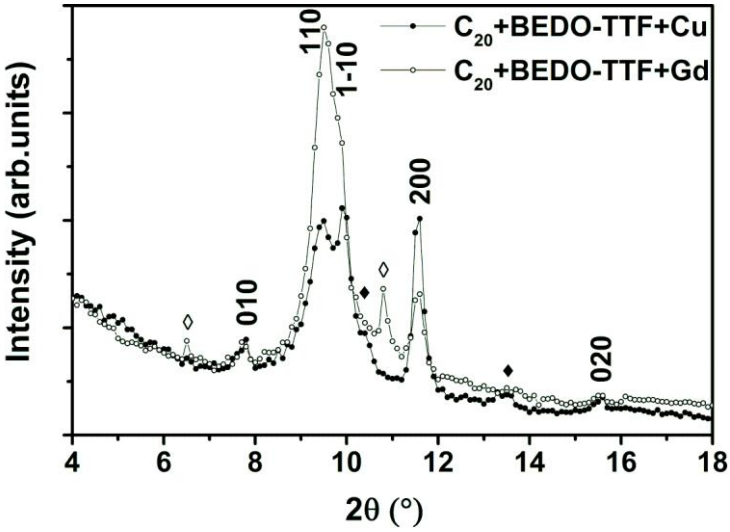

Figure 5.12. In-plane XRD patterns of 22-layer thick LB films of C_{20} + BEDO-TTF + Cu deposited at ∏ = 35 mN/m (●) and C_{20} + BEDO-TTF + Gd deposited at ∏ = 15 mN/m (○). Un-indexed peaks in the XRD spectrum are indicated by the symbol ◊ (♦) for the C_{20} + BEDO-TTF + Gd (C_{20} + BEDO-TTF + Cu) LB film.

The in-plane diffraction patterns indicate that both hybrid LB films have a similar in-plane crystal structure despite of the large differences in the out-of-plane periodic unit dimension (*d*) in the growth direction. Hence the intermolecular separation within BEDO-TTF sheet must be the same in the two LB films and the charge transfer characteristics of BEDO-TTF molecules in the C_{20} + BEDO-TTF + Gd LB film seem to be altered by the C_{20}/BEDO-TTF interface only.

5.3.5. Transmission electron microscopy investigations

To obtain further information on the position of the metal ions in the LB films high resolution TEM measurements were carried out on 140-layer thick hybrid LB films deposited on mylar substrates. HRTEM and HAADF-STEM images of the C_{20} + BEDO-TTF + Gd LB film are presented in figure 5.13 and clearly showed the layered structure. The dark contrast in HRTEM and the bright contrast in HAADF-STEM image are due to Gd as demonstrated by the STEM-EDX spectra taken from the film area indicated by red spot and reported in figure 5.13 (c). However, the average size of repeat unit deduced from the line profile drawn across the layers presented as insert in figure 5.13 (a), was found to be ~ 32 Å, *i.e.* much smaller than the value of 55 Å determined from X-ray diffraction.

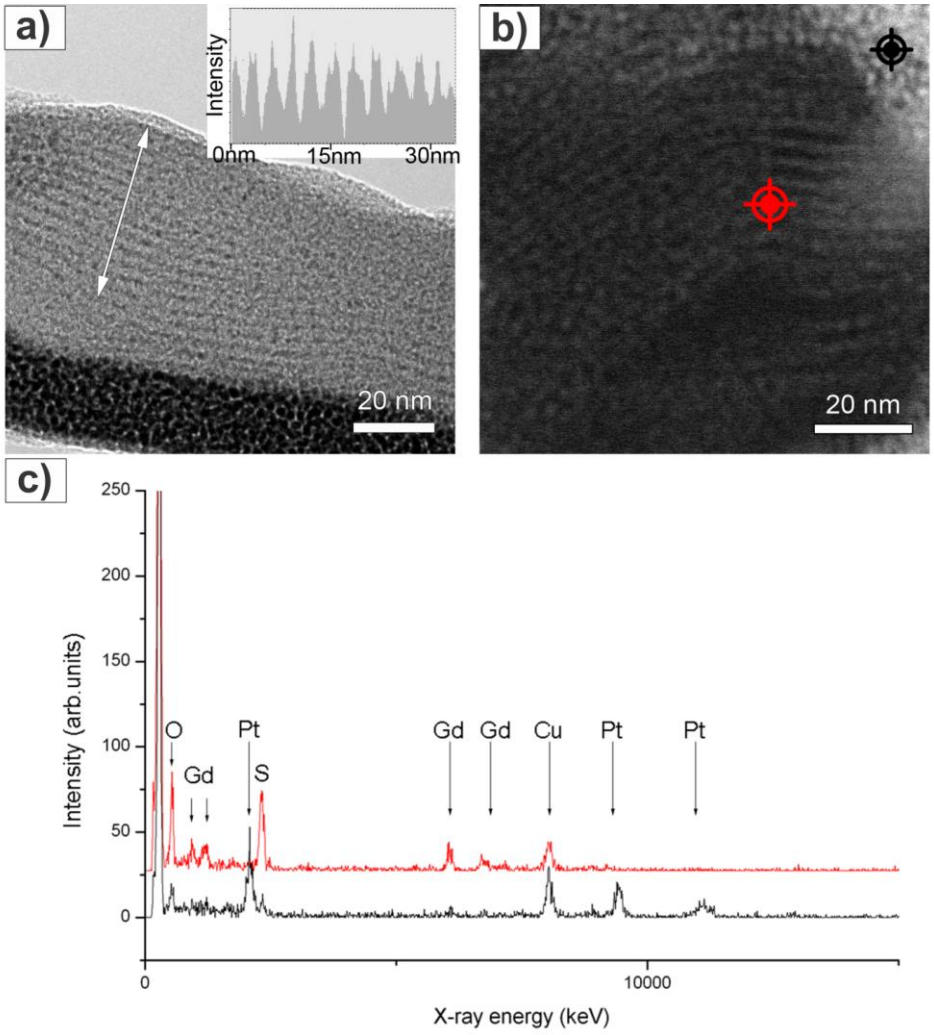

Figure 5.13. (a) HRTEM image of a cross-sectional thin lamella prepared from a 140-layer thick C_{20} + BEDO-TTF + Gd LB film; the inset shows a line profile drawn across the layers, (b) HAADF-STEM image of the same sample where Gd gives brighter contrast, and (c) STEM-EDX spectra taken on the film and the Pt protection layer as indicated respectively by red and black spots in (b).

This indicates damage in organic layers as a result of focused ion beam (FIB) milling used to prepare the cross-sectional thin lamella. Light materials such as organic structures are sensitive to the ion bombardment to thin the lamella. While in the case of the C_{20} + BEDO-TTF + Gd LB film, the film is only partially destroyed allowing for the TEM measurements

to testify to the presence of an inorganic layer sandwiched between organic ones, the damage was much more severe in the case of the C_{20} + BEDO-TTF + Cu LB film which resulted to be completely amorphous during TEM inspection after the preparation of the lamella.

5.4. Conclusion

The results presented here demonstrate the successful deposition of functional organic molecules and inorganic species in layer-by-layer fashion with smooth interfaces. The film deposition strategy presented here is sufficiently versatile to build up ordered heterostructures with a good control of the structure built up during the growth. The molecular organization within the organic layer and hence the functional properties of the hybrid systems can be manipulated with the choice of inorganic species. Hence by selecting magnetic ions with different size and oxidation state, novel architectures can be created at room temperature. The functional properties of the C_{20}+BEDO-TTF+Gd and C_{20}+BEDO-TTF+Gd LB films will be presented in next chapter where we discuss the electrical transport measurements and the magnetic characteristics.

References

(1) Coronado, E.; Galan-Mascaros, J. R.; Gomez-Garcia, C. J.; Laukhin, V. *Nature* **2000**, *408*, 447.

(2) Ojima, E.; Fujiwara, H.; Kato, K.; Kobayashi, H.; Tanaka, H.; Kobayashi, A.; Tokumoto, M.; Cassoux, P. *Journal of the American Chemical Society* **1999**, *121*, 5581.

(3) Zhang, B.; Tanaka, H.; Fujiwara, H.; Kobayashi, H.; Fujiwara, E.; Kobayashi, A. *Journal of the American Chemical Society* **2002**, *124*, 9982.

(4) Kobayashi, H.; Tomita, H.; Naito, T.; Kobayashi, A.; Sakai, F.; Watanabe, T.; Cassoux, P. *Journal of the American Chemical Society* **1996**, *118*, 368.

(5) Kobayashi, H.; Cui, H.; Kobayashi, A. *Chemical Reviews (Washington, DC, United States)* **2004**, *104*, 5265.

(6) Parkin, S. S. P.; Engler, E. M.; Lee, V. Y.; Schumaker, R. R. *Molecular Crystals and Liquid Crystals* **1985**, *119*, 375.

(7) Williams, J. M.; Emge, T. J.; Wang, H. H.; Beno, M. A.; Copps, P. T.; Hall, L. N.; Carlson, K. D.; Crabtree, G. W. *Inorganic Chemistry* **1984**, *23*, 2558.

(8) Williams, J. M.; Schultz, A. J.; Geiser, U.; Carlson, K. D.; Kini, A. M.; Wang, H. H.; Kwok, W.-K.; Whangbo, M.-H.; Schirber, J. E. *Science* **1991**, *252*, 1501.

(9) Day, P.; Kurmoo, M.; Mallah, T.; Marsden, I. R.; Friend, R. H.; Pratt, F. L.; Hayes, W.; Chasseau, D.; Gaultier, J. *Journal of the American Chemical Society* **1992**, *114*, 10722.

(10) Coronado, E.; Giménez-Saiz, C.; Gómez-García, C. J.; Capelli, S. C. *Angewandte Chemie* **2004**, *116*, 3084.

(11) Wang, L.; Yoon, M.-H.; Lu, G.; Yang, Y.; Facchetti, A.; Marks, T. J. *Nature Materials* **2006**, *5*, 893.

(12) Yang, Z.; Lange, M.; Volodin, A.; Szymczak, R.; Moshchalkov, V. V. *Nature Materials* **2004**, *3*, 793.

(13) Dusastre, V. J. *Nature Materials* **2012**, *11*, 745.

(14) Prigodin, V. N.; Raju, N. P.; Pokhodnya, K. I.; Miller, J. S.; Epstein, A. J. *Advanced Materials* **2002**, *14*, 1230.

(15) Yoo, J.-W.; Chen, C.-Y.; Jang, H. W.; Bark, C. W.; Prigodin, V. N.; Eom, C. B.; Epstein, A. J. *Nature Materials* **2010**, *9*, 638.

(16) Petty, M. C. *Langmuir-Blodgett Films*; Cambridge University Press, 1996.

(17) Makiura, R.; Motoyama, S.; Umemura, Y.; Yamanaka, H.; Sakata, O.; Kitagawa, H. *Nature Materials* **2010**, *9*, 565.

(18) Töllner, K.; Popovitz-Biro, R.; Lahav, M.; Milstein, D. *Science* **1997**, *278*, 2100.

(19) Qian, D.-J.; Nakamura, C.; Miyake, J. *Langmuir* **2000**, *16*, 9615.

(20) Akhtar, N.; Gengler, R. Y. N.; Palstra, T. T. M.; Rudolf, P. *The Journal of Physical Chemistry C* **2012**, *116*, 24130.

(21) Penacorada, F.; Reiche, J.; Katholy, S.; Brehmer, L.; Rodriguez-Mendez, M. L. *Langmuir* **1995**, *11*, 4025.

(22) Friedenberg, M. C.; Fuller, G. G.; Frank, C. W.; Robertson, C. R. *Langmuir* **1996**, *12*, 1594.

(23) Ohnuki, H.; Desbat, B.; Giffard, M.; Izumi, M.; Imakubo, T.; Mabon, G.; Delhaes, P. *The Journal of Physical Chemistry B* **2001**, *105*, 4921.

(24) McIntyre, N. S.; Cook, M. G. *Analytical Chemistry* **1975**, *47*, 2208.

(25) Barr, T. L. *Journal of Vacuum Science & Technology A: Vacuum, Surfaces, and Films* **1991**, *9*, 1793.

(26) Raiser, D.; Deville, J. P. *Journal of Electron Spectroscopy and Related Phenomena* **1991**, *57*, 91.

(27) Mullica, D. F.; Lok, C. K. C.; Perkins, H. O.; Benesh, G. A.; Young, V. *Journal of Electron Spectroscopy and Related Phenomena* **1995**, *71*, 1.

(28) Szade, J.; Neumann, M.; Karla, I.; Schneider, B.; Fangmeyer, F.; Matteucci, M. *Solid State Communications* **2000**, *113*, 709.

(29) Lademan, W. J.; See, A. K.; Klebanoff, L. E.; van der Laan, G. *Physical Review B* **1996**, *54*, 17191.

(30) Gelius, U.; Heden, P.; Hedman, J.; Lindberg, B.; Manne, R.; Nordberg, R.; Nordling, C.; Siegbahn, K. *Physica Scripta* **2007**, *2*, 70.

(31) Gupta, J. A.; Landheer, D.; Sproule, G. I.; McCaffrey, J. P.; Graham, M. J.; Yang, K. C.; Lu, Z. H.; Lennard, W. N. *Applied Surface Science* **2001**, *173*, 318.

(32) Itti, R.; Mori, H.; Ikeda, K.; Hirabayashi, I.; Koshizuka, N.; Tanaka, S. *Physica C: Superconductivity* **1991**, *185–189, Part 4*, 2673.

(33) Wagner, C.; Muilenberg, G. *Handbook of X-ray Photoelectron Spectroscopy*; Perkin-Elmer, 1979.

(34) Moldenhauer, J.; Pokhodnia, K. I.; Schweitzer, D.; Heinen, I.; Keller, H. J. *Synthetic Metals* **1993**, *56*, 2548.

(35) Pietsch, U.; Holy, V.; Baumbach, T. *High-Resolution X-ray Scattering: from Thin Films to Lateral Nanostructures*; Springer, 2004.